S1. Dynamic conductivity and optical absorption of graphene

S1.A. Estimating the Fermi level in CVD grown graphene

The Raman spectra are shown in Figure 1b and Figure S1a. The *G* and *2D* band peaks are excited by a 514 nm laser and are located at 1582 cm^{-1} and 2698 cm^{-1} respectively. The Raman spectra are homogeneous within one device, and vary less than 5 cm^{-1} from sample to sample. The Lorentzian lineshape with full-width half-maximum of the *G* (34.9 cm^{-1}) and *2D* (49.6 cm^{-1}) band indicates the graphene monolayer [S1]. The phonon transport properties are represented by the *G* and *2D* peak positions (varying within 1 cm^{-1} over the sample) and the intensity ratios between the *G* and *2D* peaks (fluctuating from 1 to 1.5) which indicate single monolayer and $\sim 5 \times 10^{12}$ cm^{-2} *p*-doping densities. Good uniformity of graphene is also confirmed by the symmetrical single Raman *G* peak [S2].
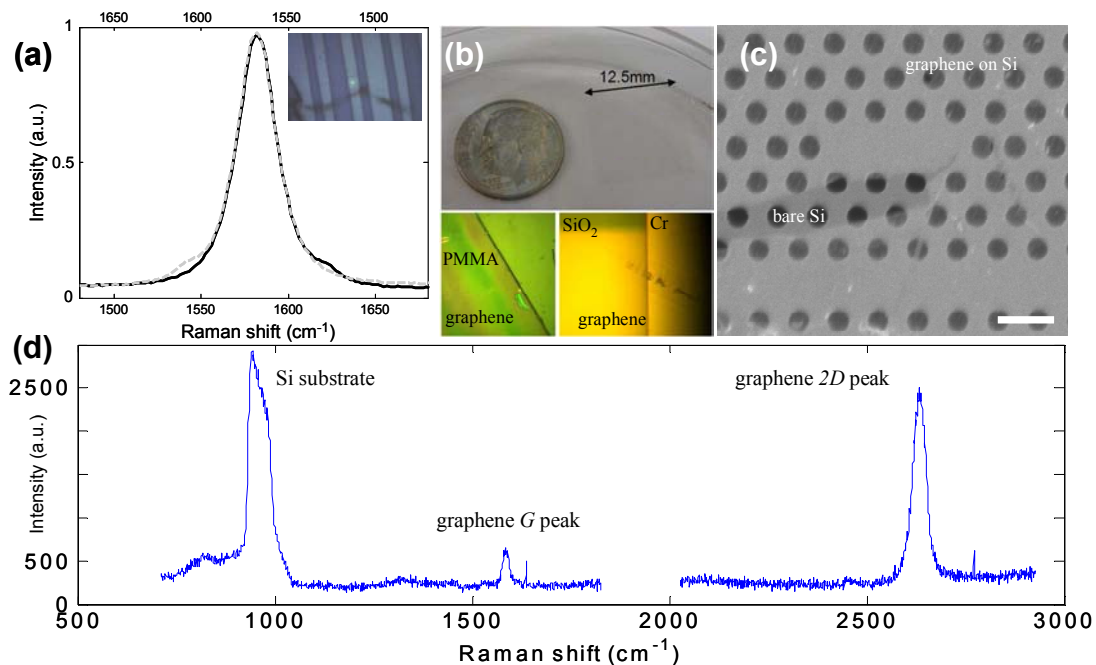

Figure S1 | Raman spectrum and transferred graphene samples. a, Raman *G* peak (black line) and its inverse (grey dashed line) to illustrate *G* peak symmetry. Inset: optical micrograph of the device with graphene transferred under Raman measurement. **b,** A centimeter-scale graphene film prepared. Optical micrograph of graphene film transferred to various substrates (poly-methyl methacrylate), air-bridged silicon membranes, silicon oxide and partially covered metal surfaces), with graphene

interface pictured. **c,** scanning electronic micrograph of example air-bridged device sample with graphene covering the whole area except the dark (exposed) region. Scale bar: 500 nm. **d,** Complete Raman spectrum of the graphene-cladded silicon membrane samples.

Figure S1b and S1c illustrates example transfers of large-area CVD graphene into various substrates including poly(methyl methacrylate) [PMMA], air-bridged silicon membranes, silicon oxide, and partially covered metal surfaces. CVD grown graphene is thicker and has rough surfaces compared to exfoliated graphene, shown by the broadened *2D* peak and the fluctuation of the *2D* versus *G* peak ratio [S3]. The thickness of graphene is ~ 1 nm. Wrinkles on the graphene surface are formed during the cool down process, due to the differential thermal expansion between the copper substrate and graphene, and consistently appear only at the edges of our samples. We emphasize that at the device regions most of the devices are covered with a single unwrinkled graphene layer.

The *2D* peak is observable only when the laser excitation energy (E_L) and the energy corresponding to electron-hole recombination process (E_T) follow the relation: (E_L-E_T)/2 >E_F, where E_F is the Fermi energy of graphene. With 514 nm laser excitation, the *2D* peak is located at 2698 cm^{-1} (Figure 1b and Figure S1a).

We note that wet transfer of graphene is used in these measurements. While a very thin (in the range of nanometers) residual layer of PMMA can remain on the sample after transfer, PMMA typically only has a non-centrosymmetric $\chi^{(2)}$ response with a negligible $\chi^{(3)}$ response and hence does not contribute to the enhanced four-wave mixing observations. The dopants can arise from residual absorbed molecules or ions on graphene or at the grain boundaries, during the water bath and transfer process. With the same CVD growth process, we also examined the dry transfer technique which controls the doping density to be low enough such that the Fermi level is within the interband optical transition region. In that case, the measured samples have a significantly increased fiber-chip-fiber coupling loss from ~0dB to ~ 11 dB over the 120 µm length photonic crystal waveguide (~0.01dB/µm).The wet transfer technique significantly reduced the linear absorption, thereby allowing the various nonlinear optoelectronic measurements first observed in this work.

S1.B. Calculations of graphene's dynamic conductivity

Given the fact that CVD graphene is heavily p-doped, the dynamic conductivity for intra- and inter-band optical transitions [S4] can be determined from the Kubo formalism as:

$$\sigma_{\text{intra}}(\omega) = \frac{je^2\mu}{\pi\hbar(\omega + j\tau^{-1})} \quad , \tag{S-E1}$$

$$\sigma_{\text{inter}}(\omega) = \frac{je^2\mu}{4\pi\hbar}\ln(\frac{2\,|\,\mu\,|-\hbar(\omega + j\tau^{-1})}{2\,|\,\mu\,|+\hbar(\omega + j\tau^{-1})}), \tag{S-E2}$$

where e is the electron charge, $\hbar$ is the reduced Plank constant, ω is the radian frequency, μ is chemical potential, and τ is the relaxation time (1.2 ps for interband conductivity and 10 fs for intraband conductivity). The dynamic conductivity of intra- and inter-band transitions at 1560 nm are $(-0.07-0.90i)\times10^{-5}$ and $(4.15-0.95i)\times10^{-5}$ respectively, leading to the total dynamic conductivity $\sigma_{total}=\sigma_{intra}+\sigma_{inter}$ of $(4.1-1.8i)\times10^{-5}$. Given negative imaginary part of total conductivity, the TE mode is supported in graphene [S5]. The light can travel along the graphene sheet with weak damping and thus no significant loss is observed for the quasi-TE mode confined in the cavity [S6]. The impurity density of the 250 nm silicon membrane is ~10^{11} cm^{-2}, slightly lower than the estimated doping density in graphene: ~5×10^{12} cm^{-2}).

S2. Parameter space of nonlinear optics in graphene nanophotonics

Figure S2 compares cavity-based switching and modulation across different platforms including silicon, III-V and the hybrid graphene- silicon cavities examined in this work. The thermal or free-carrier plasma-based switching energy is given by $P_{0th/e}\times\tau_{th/e}$, where $P_{0th/e}$ is the threshold laser power required to shift the cavity resonance half-width through thermal or free carrier dispersion; $\tau_{th/e}$ are the thermal and free-carrier lifetimes in resonator. Note that the lifetime should be replaced by cavity photon lifetime if the latter is larger (for high Q cavity). Graphene brings about a lower switching energy due to strong two-photon absorption (~3,000 cm/GW) [S7]. The recovery times of thermal switching (in red) are also shortened due to higher thermal conductivity in graphene, which is measured for supported graphene monolayers at 600 W/mK [S8] and bounded only by the graphene-contact interface and strong interface phonon scattering.
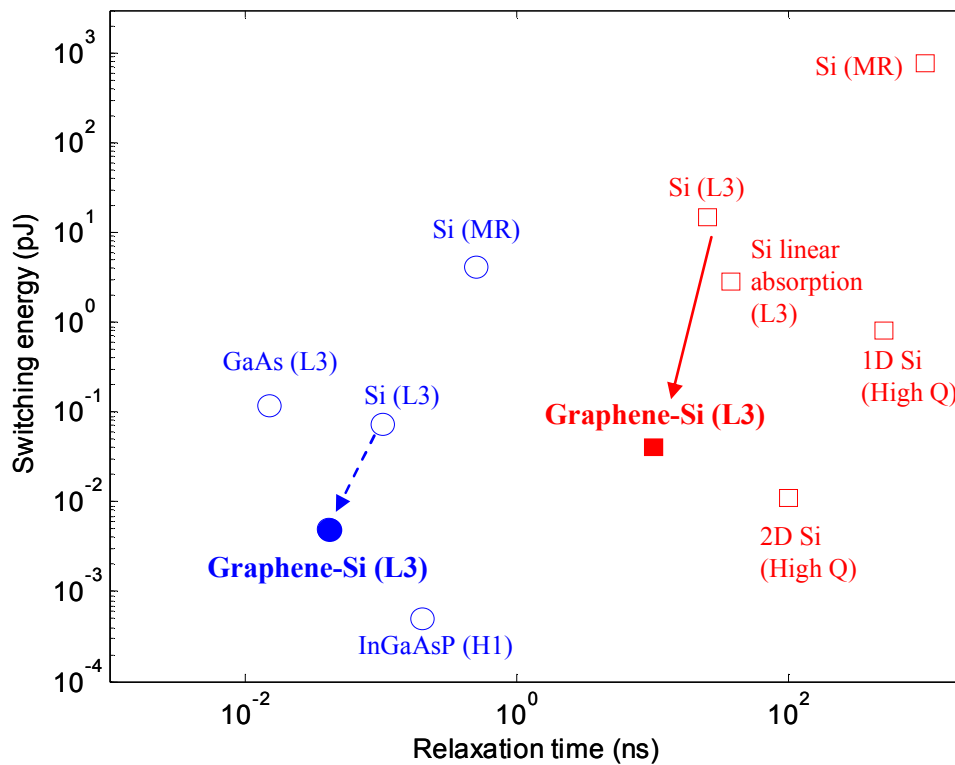
Figure S2 | Comparison of switching energy versus recovery time of cavity-based modulators and switches across different semiconductor material platforms. The blue circles are carrier plasma-induced switches with negative detuning, and the red squares are thermal-optic switches with positive detuning. The dashed lines illustrate the operating switch energies versus recovery times, for the same material [S9-16]. *L3* (*H1*) denotes photonic crystal *L3* (*H1*) cavity; *MR* denotes microring resonator.

The switching energy is inversely proportional to two photon absorption rate (β_2). Table I below summarizes the first-order estimated physical parameters from: (1) coupled-mode theory and experimental data matching; (2) full three-dimensional numerical field simulations, and (3) directly measured data, further detailed in the various sections of this Supplementary Information. With the enhanced two-photon absorption in graphene and first-order estimates of the reduced carrier lifetimes (detailed in Section S3), the switching energy – recovery time performance of the hybrid graphene-silicon cavity is illustrated in Figure S2, compared to monolithic GaAs or silicon ones.

TABLE I | Estimated physical parameters from time-dependent coupled-mode theory-experimental matching, three-dimensional numerical field simulations, and measurement data.

Parameter	Symbol	GaAs [S17]	Si	Monolayer Graphene-Si
TPA coefficient	β_2 (cm/GW)	10.2	1.5 [S18]	25[3D]
Kerr coefficient	n_2 (m^2/W)	1.6×10-17	0.44×10^{-17} [S18]	7.7×10^{-17} [3D]
Thermo-optic coeff.	dn/dT	2.48×10-4	1.86×10^{-4}	
Specific heat	$c_v\rho$(W/Km^{-3})	1.84×106	1.63×10^6 [cal]	
Thermal relaxation time	$\tau_{th,c}$ (ns)	8.4	12	10 [cal]
Thermal resistance	R_{th} (K/mW)	75	25 [19]	20 [cal]
FCA cross section	σ ($10^{-22}m^3$)	51.8	14.5	
FCD parameter	ζ ($10^{-28}m^3$)	50	13.4	
Carrier lifetime	τ_{fc} (ps)	8	500 [S20]	200 [CMT]
Loaded Q	Q	7000	7000 [m]	
Intrinsic Q	Q_0	30,000	23,000 [m]	

[CMT]: nonlinear time-dependent coupled mode theory simulation; [3D]: three-dimensional numerical field calculation averages; [m]: measurement at low power; [cal]: first-order hybrid graphene-silicon media calculations. τ_{fc} is the effective free-carrier lifetime accounting for both recombination and diffusion.

S3. Graphene two-photon absorption and accompanying thermal and free-carrier nonlinearities

With increasing input power, the transmission spectra evolve from symmetric Lorentzian to asymmetric lineshapes as illustrated in the examples of Figure 1d and Figure S3. Through second-order perturbation theory [S7], the two-photon absorption coefficient β_2 in monolayer graphene is estimated through the second-order interband transition probability rate per unit area as:

$$\beta_2 = \frac{4\pi^2}{\varepsilon_\omega \omega^4 \hbar^3}\left(\frac{v_F e^2}{c}\right)^2 ,$$

(S-E3)

where v_F is the Fermi velocity, $\hbar$ is the reduced Planck's constant, e is the electron charge, and ε_ω is the permittivity of graphene in the given frequency. At our 1550 nm wavelengths, β_2 is determined through Z-scan measurements and first-principle calculations to be in the range of ~ 3,000 cm/GW [S7].

We track the L3 cavity resonance in the transmission spectra with different input powers as illustrated in Figure S3. With thermal effects, the cavity resonance red-shifts

1.2 nm/mW for the graphene-cladded sample ($Q \sim 7,000$) and only 0.3 nm/mW for silicon sample (similar $Q \sim 7,500$). These sets of measurements are summarized in Figure S3c where the thermal red-shift is sizably larger in the graphene-cladded sample versus a near-identical monolithic silicon cavity. In addition, Figure S3d shows the tuning efficiency for a range of cavity Qs examined in this work – with increasing Q the monolithic silicon cavity shows an increase in tuning efficiency while the converse occurs for the graphene-silicon cavity. Figure S4a shows the steady-state bistable hysteresis for more detunings, and Figure S4b shows the temporal switching with an illustrative detuning of -0.8 and 0.6 nm.
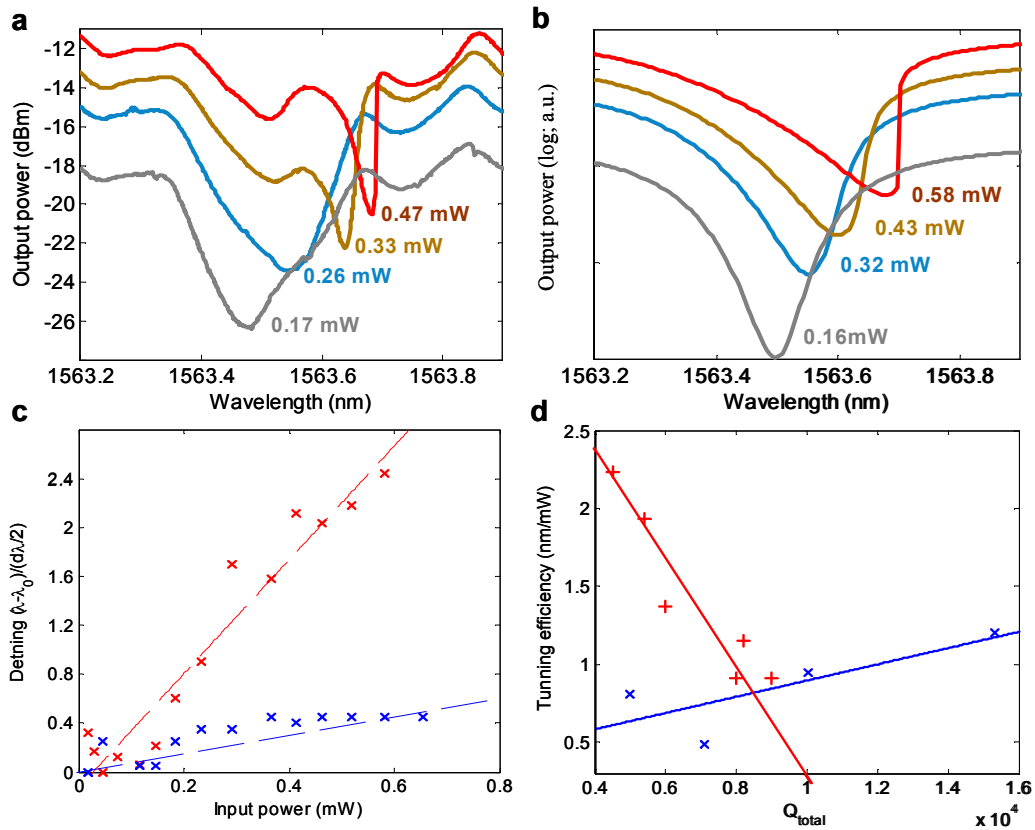

Figure S3 | Steady-state two-photon absorption induced thermal nonlinearities in graphene-silicon hybrid cavities. a, Measured quasi-TE transmission spectra of a graphene-cladded L3 cavity with different input power levels (with extracted insertion loss from the facet of waveguides in order to be comparable to simulation in b). **b,** Nonlinear coupled mode theory simulated transmission spectra. The estimated input powers are marked in the panels. **c,** Measured cavity resonance shifts versus input power, with the graphene-cladded cavity samples (in red) and the monolithic silicon control cavity sample (in blue). **d,** Tuning efficiencies for graphene-cladded cavity samples (in red) and control cavity samples (in blue) for a range of cavity loaded Q-factors examined.
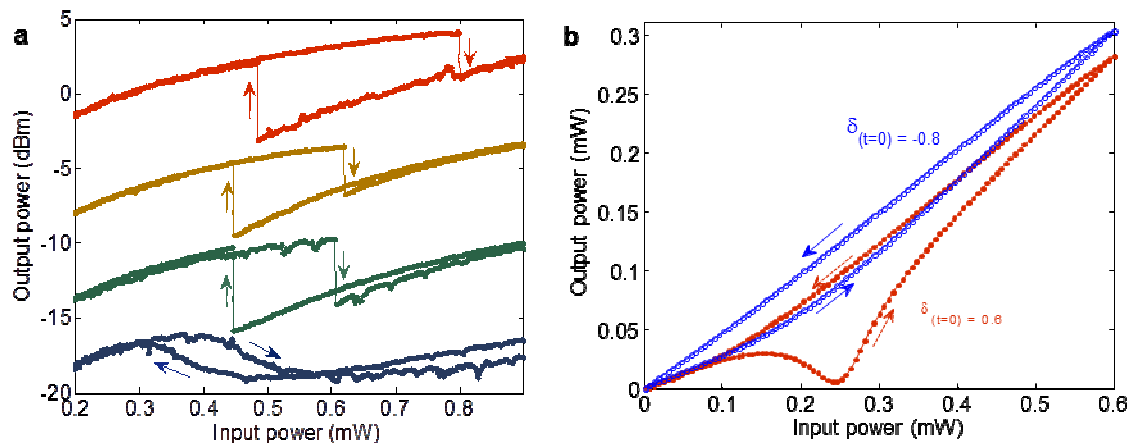
Figure S4 | Bistable switching in graphene-cladded nanocavities. a, Measured steady-state bistability at different detunings set at 0.18, 0.23, 0.26, 0.29 nm (from bottom to top). The plots are offset for clarity: green (offset 2 dB), brown (offset 8 dB) and red lines (offset 15 dB). **b,** Coupled-mode equations calculated switching dynamics with triangular input. The output power versus input power for the positive (red) and negative (blue) detuning with triangular input.

We model the nonlinear cavity transmissions with time-domain nonlinear coupled mode theory for the temporal rate evolution of the photon, carrier density and temperatures as described by [S21]:

$$\frac{da}{dt} = (i(\omega_L - \omega_0 + \Delta\omega) - \frac{1}{2\tau_t})a + \kappa\sqrt{P_{in}} , \qquad \text{(S-E4)}$$

$$\frac{dN}{dt} = \frac{1}{2\hbar\omega_0\tau_{TPA}}\frac{V_{TPA}}{V_{FCA}^2}|a|^4 - \frac{N}{\tau_{fc}} , \qquad \text{(S-E5)}$$

$$\frac{d\Delta T}{dt} = \frac{R_{th}}{\tau_{th}\tau_{FCA}}|a|^2 + \frac{\Delta T}{\tau_{th}} , \qquad \text{(S-E6)}$$

where a is the amplitude of resonance mode; N is the free-carrier density; ΔT is the cavity temperature shift. P_{in} is the power carried by incident continuous-wave laser. κ is the coupling coefficient between waveguide and cavity, adjusted by the background Fabry-Perot resonance in waveguide [S22]. $\omega_L-\omega_0$ is the detuning between the laser frequency (ω_L) and cold cavity resonance (ω_0). The time-dependent cavity resonance shift is $\Delta\omega=\Delta\omega_N-\Delta\omega_T+\Delta\omega_K$, where the free carrier dispersion is $\Delta\omega_N=\omega_0\zeta N/n$. The thermal induced dispersion is $\Delta\omega_T=\omega_0\Delta T(dn/dT)/n$. $\Delta\omega_K$ is the Kerr dispersion, and is negligibly small compared to the thermal and free-carrier mechanisms.

The total loss rate is $1/\tau_t = 1/\tau_{in} + 1/\tau_v + 1/\tau_{lin} + 1/\tau_{TPA} + 1/\tau_{FCA}$. $1/\tau_{in}$ and $1/\tau_v$ is the loss rates into waveguide and vertical radiation into the continuum, $(1/\tau_{in/v} = \omega/Q_{in/v})$, the linear absorption $1/\tau_{lin}$ for silicon and graphene are demonstrated to be small. The free carrier absorption rate $1/\tau_{FCA} = c\sigma N(t)/n$. The field averaged two-photon absorption rate $1/\tau_{TPA} = \overline{\beta_2} c^2/n^2/V_{TPA}|a|^2$, where the effective two-photon absorption coefficient is defined as:

$$\overline{\beta_2} = (\frac{\lambda_0}{2\pi})^d \frac{\int n^2(r)\beta_2(r)(|E(r)\cdot E(r)|^2 + 2|E(r)\cdot E(r)^*|^2)d^d r}{(\int n^2(r)|E(r)|^2 \, d^d r)^2} , \text{(S-E7)}$$

The mode volume for two-photon absorption (same as Kerr):

$$V_{TPA/Kerr} = \frac{(\int n^2(r)|A(r)|^2 \, dr^3)^2}{\int_{Si} n^4(r)|A(r)|^4 \, dr^3} , \qquad \text{(S-E8)}$$

The effective mode volume for free-carrier absorption is:

$$V^2_{FCA} = \frac{(\int n^2(r)|A(r)|^2 \, dr^3)^3}{\int_{Si} n^6(r)|A(r)|^6 \, dr^3} . \qquad \text{(S-E9)}$$

The model shows remarkable match to the measured transmissions. With the two-photon absorption and Kerr (Supplementary Information, Section 5) coefficients of the hybrid cavity calculated from 3D finite-difference time-domain field averages and first-order estimates of the thermal properties (specific heat, effective thermal resistance, and relaxation times), the carrier lifetime of the graphene-cladded photonic crystal cavity is estimated to first-order at 200 ps.

S4. Switching dynamics and regenerative oscillation in graphene-cladded silicon cavities

From the nonlinear coupled mode modeling, the dynamical responses of the hybrid cavity to step inputs are shown in Figure S5a, illustrating the switching dynamics and regenerative oscillations. Free carrier dispersion causes the switching on the negative-detuned laser, and the thermal nonlinearity leads to the switching on the positive side. The interplay of the free-carrier-induced cavity resonance blue-shift dynamics with the thermal-induced cavity red-shift time constants is observed. Figure S5b shows the correspondent radio frequency spectrum. By tuning the laser wavelength, the fundamental mode can be set from 48 MHz (zero detuning) to 55 MHz (0.3 nm detuning). The dependence of oscillation period to the detuning and input laser power is further provided in Figure S5c and Figure S5d respectively.
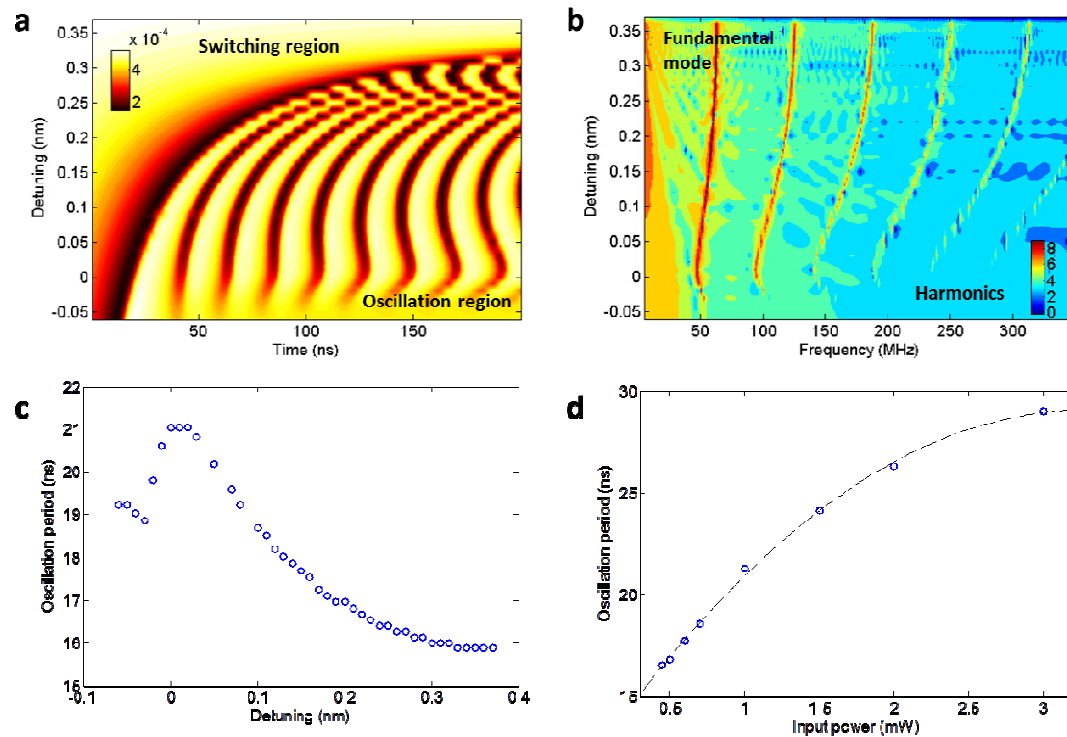
Figure S5 | Coupled-mode equations calculated time domain response to a step input with a graphene-cladded silicon photonic crystal _L3_ nanocavity side-coupled to a photonic crystal waveguide. a, The output versus input powers for positive and negative detunings (laser-cavity detunings are set from -0.06 to 0.37 nm). Input laser power is set at 0.6 mW. The cavity switching dip is observed for all detunings, and regenerative oscillation exists only predominantly for positive detuning. **b,** Frequency response of the cavity switching and oscillation dynamics with conditions as in **a** (in log scale). The laser detuning is set from -0.06 to 0.37 nm. **c** and **d.** Oscillation period versus laser detunings and input powers respectively.

Regenerative oscillations were theoretically predicted in GaAs nanocavities with large Kerr nonlinearities [S23], or observed only in high-Q silicon microdisks (Q at 3×10^5) with V at $40(\lambda/n_{Si})^3$, at sub-mW power levels [S24]. The graphene-enhanced two-photon absorption, free-carrier and thermal effects allow regenerative oscillations to be experimentally observable with Q^2/V values [of $4.3\times10^7(\lambda/n)^3$] at least 50× lower, at the same power threshold levels. The regenerative oscillations with lower Qs allow higher speed and wider bandwidth operation, and are less stringent on the device nanofabrication.

S5. Ultrafast Kerr in graphene – silicon hybrid structures

S5.A. Computations of effective Kerr nonlinearity in graphene-cladded silicon cavities

Third-order nonlinearity susceptibility for graphene is reported as large as $|\chi^{(3)}| \sim 10^{-7}$ esu in the wavelength range of 760 to 840 nm [S25]. When two external beams with frequency ω_1 (pump) and ω_2 (signal) are incident on graphene, the amplitude of sheet current generated at the harmonics frequencies ($2\omega_1 - \omega_2$) is described by:

$$j_e = -\frac{3}{32}\frac{e^2}{\hbar}\varepsilon_2 \left(\frac{ev_F\varepsilon_1}{\hbar\omega_1\omega_2}\right)^2 \frac{2\omega_1^2 + 2\omega_1\omega_2 - \omega_2^2}{\omega_1(2\omega_1 - \omega_2)} \ , \qquad \text{(S-E10)}$$

where ε_1, ε_2 are the electric field amplitudes of the incident light at frequencies ω_1 and ω_2 respectively. v_F ($= 10^6$ m/s) is the Fermi velocity of graphene. Under the condition that both ω_1 and ω_2 are close to ω, the sheet conductivity can be approximated as:

$$\sigma^{(3)} = \frac{j_e}{\varepsilon_1\varepsilon_1\varepsilon_2} = -\frac{9}{32}\frac{e^2}{\hbar}\left(\frac{ev_F}{\hbar\omega^2}\right)^2 , \qquad \text{(S-E11)}$$

Since most of the sheet current is generated in graphene, the effective nonlinear susceptibility of the whole membrane can be expressed as:

$$\chi^{(3)} = \frac{\sigma^{(3)}}{\omega d} = -\frac{9}{32}\frac{e^4 v_F^{\ 2}}{\hbar^3 c^5}\frac{\lambda^5}{d}, \qquad \text{(S-E12)}$$

where d is the thickness of the graphene (~1 nm), λ is the wavelength, and c is the speed of light in vacuum. The calculated $\chi^{(3)}$ of a monolayer graphene is in the order of 10^{-7} esu (corresponding to a Kerr coefficient $n_2 \sim 10^{-13}$ m^2/W), at 10^5 times higher than in silicon ($\chi^{(3)} \sim 10^{-13}$ esu, $n_2 \sim 4 \times 10^{-18}$ m^2/W) [S26].

Effective n_2 of the hybrid graphene-silicon membrane is then calculated for an inhomogeneous cross-section weighted with respect to field distribution [S27]. With a baseline model without complex graphene-surface electronic interactions, the effective n_2 can be expressed as:

$$\overline{n_2} = \left(\frac{\lambda_0}{2\pi}\right)^d \frac{\int n^2(r)n_2(r)(|E(r) \cdot E(r)|^2 + 2|E(r) \cdot E(r)^*|^2)d^d r}{\left(\int n^2(r)|E(r)|^2\ d^d r\right)^2}, \qquad \text{(S-E13)}$$

where $E(r)$ is the complex fields in the cavity and $n(r)$ is local refractive index. The local Kerr coefficient $n_2(r)$ is 3.8×10^{-18} m^2/W in silicon membrane and $\sim 10^{-13}$ m^2/W for graphene, λ_0 is the wavelength in vacuum, and $d=3$ is the number of dimensions. The complex electric field $E(r)$ is obtained from 3D finite-difference time-domain computations of the optical cavity examined [S28]. The resulting field-balanced effective n_2 is calculated to be 7.7×10^{-17} m^2/W ($\chi^{(3)} \sim 10^{-12}$esu), close to the best reported chalcogenide photonic crystal waveguides [S29, S30].

TABLE II | Field-balanced third-order nonlinear parameter.

Computed parameters	$\overline{n_2}$ (m^2/W)	$\overline{\beta_2}$ (m/W)
Graphene	10^{-13}	10^{-7}
Silicon	3.8×10^{-18}	8.0×10^{-12}
Monolayer graphene-silicon	7.7×10^{-17}	2.5×10^{-11}
Chalcogenide waveguide	7.0×10^{-17}	4.1×10^{-12}

Likewise, the effective two-photon absorption coefficient is computed in the same field-balanced approach, with a result of 2.5×10^{-11}m/W. The resulting nonlinear parameter γ ($=\omega n_2/cA_{eff}$) is derived to be 800 W^{-1}m^{-1}, for an effective mode area of 0.25 μm^2.

S5.B. Local four-wave mixing in graphene-cladded photonic crystals cavities

The conversion efficiency of the single cavity $\eta = |\gamma P_p L'|^2 FE_p^4 FE_s^2 FE_c^2$, where FE_p, FE_s, and FE_c are the field enhancement factors of pump, signal and idler respectively [S31]. The effective length L' includes the phase mismatch and loss effects. Compared to the original cavity length ($\sim$ 1582.6 nm), the effective cavity length is only slightly modified by less than 1 nm. However, the spectral dependent field enhancement factor is the square of the cavity build-up factor $FE^2 = P_{cav}/P_{wg} = F_{cav}(U/U_{max})\eta_p^2$, where U/U_{max} is the normalized energy distribution with the Lorenzian lineshape. $\eta_p = 0.33$ is the correction term for the spatial misalignment between the quasi-TE mode and graphene, and the polarization. The field enhancement effect in the cavity is proportional to the photon mode density: $F_{cav} = Q\lambda^3/(8\pi V)$ [S32].
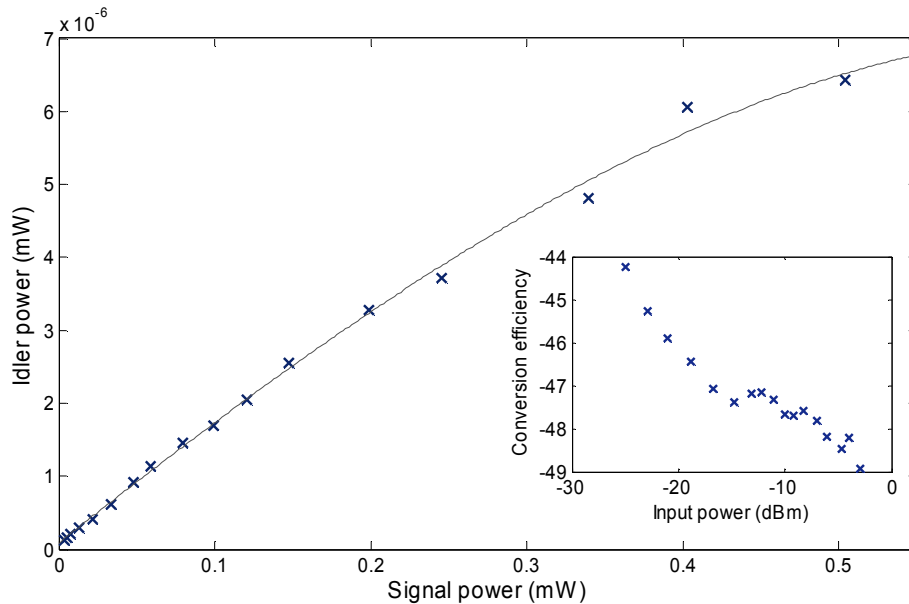
Figure S6 | Free-carrier absorption effects on the four-wave mixing conversion efficiency. Measured idler power versus signal power at the transmitted port, with the pump power is fixed on the cavity resonance and the the signal laser detuned by 200 pm. Experimental data (✕) and quadratic fit (solid line). Inset: corresponding conversion efficiency versus signal power.

The enhanced two-photon-absorption and induced free-carrier absorption would produce nonlinear loss. To investigate the direct effect of two-photon absorption and free-carrier absorption on the four wave mixing, we measure the conversion efficiency with varying input signal power as shown in Figure S6. Extra 4-dB loss is measured when the input signal power increases from -22 to -10 dBm, with the additional contribution from nonlinear absorption of the graphene-silicon cavity membrane.

Supplementary References:

[S1] A. Das, S. Pisana, B. Chakraborty, S. Piscanec, S. K. Saha, U. V. Waghmare, K. S. Novoselov, H. R. Krishnamurthy, A. K. Geim, A. C. Ferrari, and A. K. Sood, Monitoring dopants by Raman scattering in an electrochemically top-gated graphene transistor, *Nature Nanotech.* **3**, 210 (2008); C. Casiraghi, S. Pisana, K. S. Novoselov, A. K. Geim, and A. C. Ferrari, Raman fingerprint of charged impurities in graphene, *Appl. Phys. Lett.* **91**, 233108 (2007).

[S2] X. Li, W. Cai, J. An, S. Kim, J. Nah, D. Yang, R. Piner, A. Velamakanni, I. Jung, E. Tutuc, S. K. Banerjee, L. Colombo, and R. S. Ruoff, Large-area synthesis of

high-quality and uniform graphene films on copper foils, *Science* **324**, 1312 (2009).

[S3] W. Zhao, P. H. Tan, J. Liu, and A. C. Ferrari, Intercalation of few-layer graphite flakes with $FeCl_3$: Raman determination of Fermi level, layer by layer decoupling, and stability, *J. Am. Chem. Soc.* **133**, 5941 (2011).

[S4] K.F. Mak, M.Y. Sfeir, Y. Wu, C.H. Lui, J.A. Misewich, and T.F. Heinz, Measurement of the Optical Conductivity of Graphene, *Phys. Rev. Lett.* **101**, 196405 (2008).

[S5] Q. Bao, H. Zhang, B. Wang, Z. Ni, C. H. Y. X. Lim, Y. Wang, D. Yuan Tang, and K. P. Loh, Broadband graphene polarizer, *Nature Photon.* **5**, 411 (2011).

[S6] S. Mikhailov and K. Ziegler, New electromagnetic mode in graphene. *Phys. Rev. Lett.* **99**, 016803 (2007).

[S7] H. Yang, X. Feng, Q. Wang, H. Huang, W. Chen, A. T. S. Wee, and W. Ji, Giant two-photon absorption in bilayer graphene, *Nano Lett.* **11**, 2622 (2011).

[S8] J. H. Seol, I. Jo, A. L. Moore, L. Lindsay, Z. H. Aitken, M. T. Pettes, X. Li, Z. Yao, R. Huang, D. Broido, N. Mingo, R. S. Ruoff, and L. Shi, Two-dimensional phonon transport in supported graphene, *Science* **328**, 213 (2010).

[S9] T. Tanabe, M. Notomi, S. Mitsugi, A. Shinya, and E. Kuramochi, Fast bistable all-optical switch and memory on a silicon photonic crystal on-chip, *Opti. Lett.* **30**, 2575 (2005).

[S10] M. Notomi, A. Shinya, S. Mitsugi, G. Kira, E. Kuramochi, and T. Tanabe, Optical bistable switching action of Si high-Q photonic-crystal nanocavities, *Opt. Express* **13**, 2678 (2005).

[S11] L.-D. Haret, T. Tanabe, E. Kuramochi, and M. Notomi, Extremely low power optical bistability in silicon demonstrated using 1D photonic crystal nanocavity, *Optics Express* **17**, pp. 21108 (2009).

[S12] K. Nozaki, T. Tanabe, A. Shinya, S. Matsuo, T. Sato, H. Taniyama, and M. Notomi, Sub-femtojoule all-optical switching using a photonic crystal nanocavity, *Nature Photon.* **4**, 477 (2010).

[S13] C. Husko, A. De Rossi, S. Combrié, Q. V. Tran, F. Raineri, and C. W. Wong, Ultrafast all-optical modulation in GaAs photonic crystal cavities, *Appl. Phys. Lett.* **94**, 021111 (2009).

[S14] S. Kocaman, X. Yang, J. F. McMillan, M. B. Yu, D. L. Kwong, and C. W. Wong, Observations of temporal group delays in slow-light multiple coupled photonic crystal cavities, *Appl. Phys. Lett.* **96**, 221111 (2010).

[S15] V. R. Almeida and M. Lipson, Optical bistability on a silicon chip, *Opt. Lett.* **29** 2387 (2004).

[S16] Q. Xu and M. Lipson, Carrier-induced optical bistability in silicon ring resonators, *Opt. Lett.* **31**, 341 (2006).

[S17] A. de Rossi, M. Lauritano, S. Combrie, Q. Vy Tran, and C. Husko, Interplay of plasma-induced and fast thermal nonlinearities in a GaAs-based photonic crystal nanocavity, *Phys. Rev. A* **79**, 043818 (2009).

[S18] Alan D. Bristow, Nir Rotenberg, and Henry M. van Driel, Two-photon absorption and Kerr coefficients of silicon for 850–2200 nm, *Appl. Phys. Lett.* **90**, 191104 (2007).

[S19] C. J. Chen, J. Zheng, T. Gu, J. F. McMillan, M. Yu, G.-Q. Lo, D.-L. Kwong, and C. W. Wong, Selective tuning of silicon photonic crystal nanocavities via laser-assisted local oxidation, *Optics Express* **19**, 12480 (2011).

[S20] P. E. Barclay, K. Srinivasan, and O. Painter, Nonlinear response of silicon photonic crystal micro-resonators excited via an integrated waveguide and fiber taper, *Opt. Express* **13**, 801 (2005).

[S21] H. A. Haus, *Waves and Fields in Optoelectronics* (Prentice-Hall, Englewood Cliffs, NJ), p. 99 (1984).

[S22] X. Yang, C. Husko, M. Yu, D.-L. Kwong, and C. W. Wong, Observation of femto-joule optical bistability involving Fano resonances in high-Q/V_m silicon photonic crystal nanocavities, *Appl. Phys. Lett.* **91**, 051113 (2007).

[S23] A. Armaroli, S. Malaguti, G. Bellanca, S. Trillo, A. de Rossi, and S. Combrié, Oscillatory dynamics in nanocavities with noninstantaneous Kerr response, *Phys. Rev. A* **84**, 053816 (2011)

[S24] T. J. Johnson, M. Borselli, and O. Painter, Self-induced optical modulation of the transmission through a high-*Q* silicon microdisk resonator, *Opt. Express* **14**, 817 (2006).

[S25] E. Hendry, P.J. Hale, J. Moger, and A. K. Savchenko, Coherent nonlinear optical response of graphene, *Phys. Rev. Lett.***105**, 097401 (2010).

[S26] M. Dinu, F. Quochi, and H. Garcia, Third-order nonlinearities in silicon at telecom wavelengths, *Appl. Phys. Lett.* **82**, 2954 (2003).

[S27] S. Afshar V. and T. M. Monro, A full vectorial model for pulse propagation in emerging waveguides with subwavelength structures part I: Kerr nonlinearity, *Optics Express* **17**, 2298 (2009).

[S28] A. F. Oskooi, D. Roundy, M. Ibanescu, P. Bermel, J. D. Joannopoulos, and S. G. Johnson, MEEP: A flexible free-software package for electromagnetic simulations by the FDTD method, *Computer Physics Communications* **181**, 687 (2010).

[S29] B. J. Eggleton, B. Luther-Davies and K. Richardson, Chalcogenide photonics, *Nature Photonics* **5**, 141 (2011).

[S30]K. Suzuki, Y .Hamachi, and T. Baba, Fabrication and characterization of chalcogenide glass photonic crystal waveguides. *Opt. Express* **17**, 22393 (2009).

[S31] P. P. Absil, J. V. Hryniewicz, B. E. Little, P. S. Cho, R. A. Wilson, L. G. Joneckis, and P.-T. Ho, Wavelength conversion in GaAs micro-ring resonators, *Opt. Lett.* **25**, 554 (2000).

[S32] R. K. Chang and A. J. Campillo, *Optical processes in microcavities*, World Scientific, Singapore, 1996.